4

Experimental and Numerical Studies of Evaporation Local Heat Transfer in Free Jet

Hasna Louahlia Gualous
Caen Basse Normandie University/LUSAC
France

1. Introduction

Jet impingement heat transfer has been used extensively in many industrial applications for cooling because it provides high local heat transfer coefficients at low flow rates. Several experimental and theoretical studies on liquid jet impingement heat transfer have been reported in the literature (Louahlia & Baonga, 2008**,** Chen et al., 2002, Lin & Ponnappan, 2004, Liu & Zhu, 2004, Pan & Webb, 1995). Numerous studies are conducted in average heat transfer, but local heat transfer analysis for steady and unsteady states has not been much attention. Jet impingement heat transfer is influenced by different physical parameters such as: (i) the velocity turbulent fluctuations (Oliphant et al. 1998, Stevens & Webb, 1989), (ii) the difference between the temperatures of inlet jet and heat exchange surface (Siba et al. 2003, MA et al. 1997), (iii) the surface geometry and the jet orientation (MA et al. 1997b, Elison & Webb, 1994), (iv) the liquid flow rate and Prandtl number (Elison & Webb, 1994, Fabbri et al. 2003, Stevens & Webb, 1993), and (v) the nozzle diameter (Stevens & Webb, 1993, 1992).

2. Hydrodynamic characteristics of the jet impinging on a horizontal surfarce

When a liquid jet impinges on a horizontal surface, three distinct regions can be identified as shown in Figure 1. The first zone is the free jet region where the flow is accelerated because of the gravitational force. The second zone is the impingement region where the interaction between the jet and the heat exchange surface produces a strong deceleration of the flow. After this zone, the liquid wets the surface and flows in a parallel direction to the heat exchange surface. Heat transfer efficiency in each zone is related to the flow velocity and its structure. In the impingement zone, jet diameter could be measured using flurescence induced laser (Baonga et al. 2006) combined to the images processing. In this method, liquid impinging the heat exchange surface is illuminated by a laser sheet in the axial direction as shown by Figure 2. Rhodamine B with low concentration must be used as the fluerescent substance added to the liquid jet. In this case, fluorescent substance becomes visible when liquid jet is illuminated with light. A CCD camera can be used to record the flow video images. Video images are treated in order to extract the profiles of the jet as shown by Figure 1.

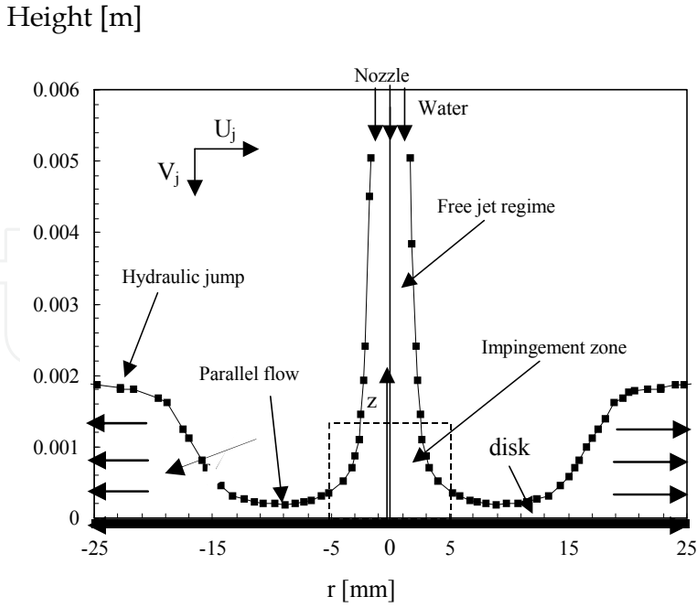

Fig. 1. Schematic of flow developing from nozzle to heated disk.

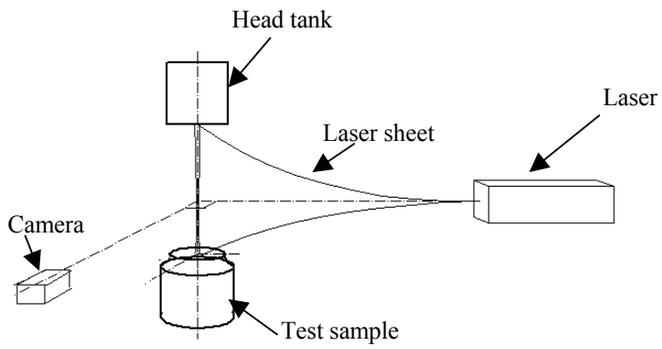

Fig. 2. Flow visualization system.

2.1 Axial flow structure

For inlet Reynolds number ranging from 1520 to 5900 (the corresponding values of the inlet mean velocity are in the range of 3.24 to 12.5 m/s), Figure 3 shows effect of the jet flow rate on the distribution of the jet diameter along the axial direction. The nozzle diameter is of 4 mm. The nozzle-heat exchange surface spacing is of 13 mm. Reynolds number is calculated as follow :

$$\mathrm{Re} = \frac{4\dot{m}}{\pi d_i \mu_L} \tag{1}$$

where: d_i is the inner diameter of the nozzle, μ_L is the dynamic viscosity, $\dot{m}$ is the total mass flow rate of the jet. Physical properties are used at the inlet jet temperature measured at the nozzle exit.

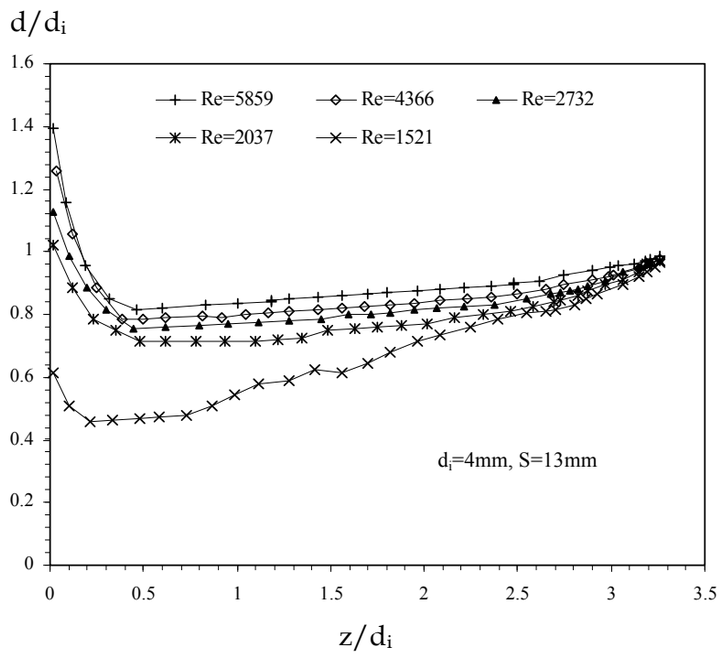

Fig. 3. Evolution of the jet diameter along the z direction.

It can be seen from figure 3 that for the same axial position (z), the jet diameter increases with inlet Reynolds number because gravitational force increases with flow velocity and becomes higher than surface tension force at the jet free surface. For lower Reynolds number (Re=1521), it shows that instability starts and waves appears on the jet free surface because capillarity force increases and becomes non-negligible compared to gravitational force.

Along the falling jet, no evaporation has been produced and the mass flow rate is conserved. In this case, axial distribution of the flow velocity can be deduced from the following equation:

$$\dot{m} = \rho_L V_j(z)\,\pi\frac{d^2(z)}{4} \tag{2}$$

At each axial position (z), $V_j(z)$ is the average velocity of the jet, $d(z)$ is the jet diameter, ρ_L is the jet density. Figure 4 shows evolution of $V_j(z)/V_{j,inlet}$ from the injection zone to the heat exchange surface for various inlets Reynolds numbers. $V_{j,inlet}$ refers liquid velocity of the jet at the nozzle exit. For each Reynolds number, velocity is high near the impingement zone where the jet diameter is low. The free jet is accelerated after the nozzle exit because the gravity force effect is very pronounced. After this zone, the jet velocity decelerates quickly because liquid flow is retained on the heat exchange surface under the effect of the capillarity force and the wall friction.

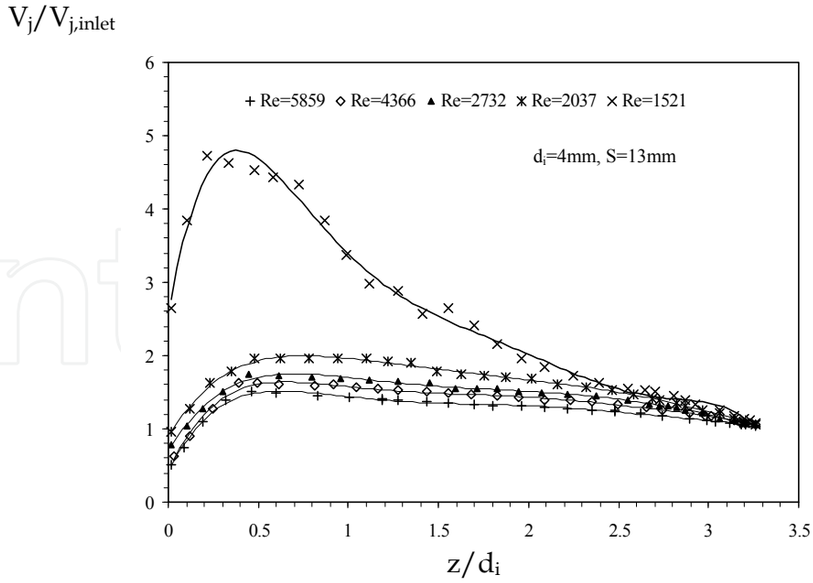

Fig. 4. Dimensionless axial velocity of the jet.

2.2 Wall parallel flow structure

Turning now to the characterisation of the local liquid layer depth near the heat exchange surface and the velocity profile along the radial direction where the heat transfer occurs.

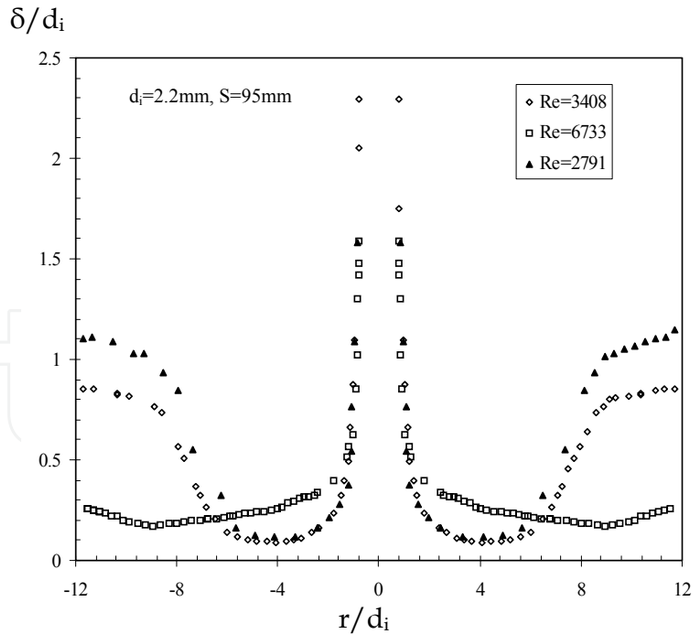

Fig. 5. Local evolution of the dimensionless liquid layer depth.

Figure 5 shows an example of the local liquid layer depth ($\delta(r)$) measured for three values of the inlet Reynolds number (Re=6733, Re=3408, and Re=2791). The nozzle diameter is of 2.2 mm for theses experiments. The jet inlet temperature is of 32°C and the nozzle-heat

exchange surface spacing is of 95 mm. Figure 5 shows three distinct zones: the impingement zone, the zone where the liquid layer depth is approximately uniform, and the final zone where a hydraulic jump is formed. The radius, at which the liquid layer depth increases, is termed as the hydraulic jump radius. For higher Reynolds number, hydraulic jump is not appeared on the heat exchange surface because it is certainly higher than the radius of the heat exchange surface. Location of hydraulic jump on the surface is an interest physical phenomenon. In the previous work, some authors (Stevens & Webb, 1992, 1993, Liu et al. 1991, 1989, Watson, 1964) show the influence of the jet mass flow rate on the hydraulic jump radius that is defined at the radius location where the liquid layer depth attains a highest value in the parallel flow (Figure 6a).

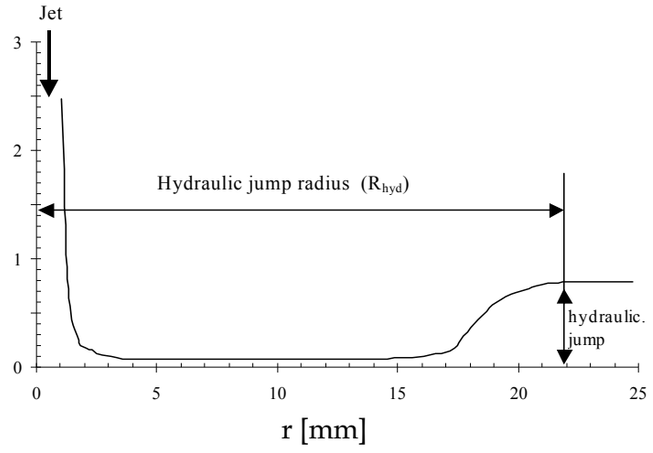

(a)

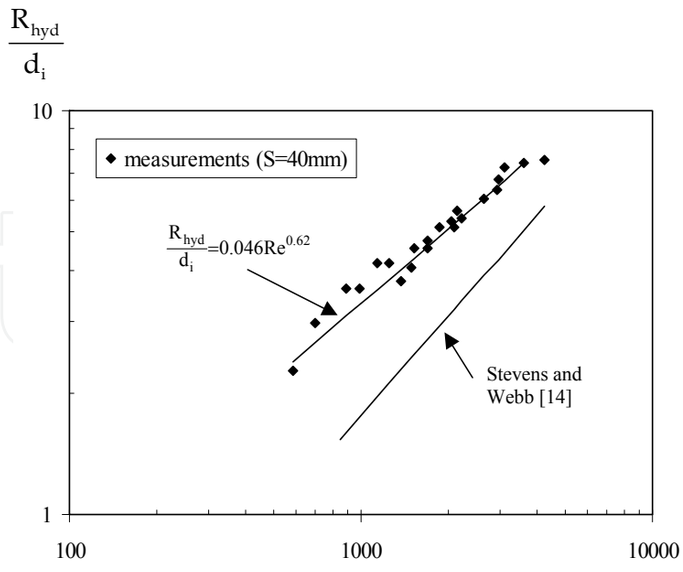

(b)

Fig. 6. a- Schematic of the hydraulic jump radius, b- Dimensionless hydraulic jump radius.

For Reynolds number ranging from 700 to 5000, Figure 6b shows dimensionless hydraulic jump radius as a function of Reynolds number. It shows that the hydraulic jump radius increases with the Reynolds number because flow is accelerated in the radial direction and the hydraulic jump is moved far from the stagnation zone. The difference between the present results and the experimental data of Stevens and Webb can be due to the uncertainty in the data of Stevens and Webb estimated of ±0.5 cm. The present results are defined with a maximum uncertainty of 2% and revealed an approximation dependence of the hydraulic jump radius on the Reynolds number as $Re^{0.62}$:

$$\frac{R_{hyd}}{d_i} = 0.046\,Re^{0.62} \tag{3}$$

Equation (3) estimates hydraulic jump radius with a maximum uncertainty of ±7%.
Distribution of the liquid velocity along the radial direction is determined by assuming conservation of the mass flow rate of liquid jet. For parallel flow:

$$\dot{m} = \rho_L U_j(r)\, 2\,\pi\, r\, \delta(r) \tag{4}$$

Where ρ_L is the jet density, $U_j(r)$ is the jet average velocity in the radial direction, r is the radial coordinate, $\delta(r)$ is the liquid layer depth on the surface.

Figure 7 shows profiles of dimensionless velocity and shows for each inlet Reynolds number, radial velocity profiles reaches a maximum value which is very pronounced for higher Reynolds number.

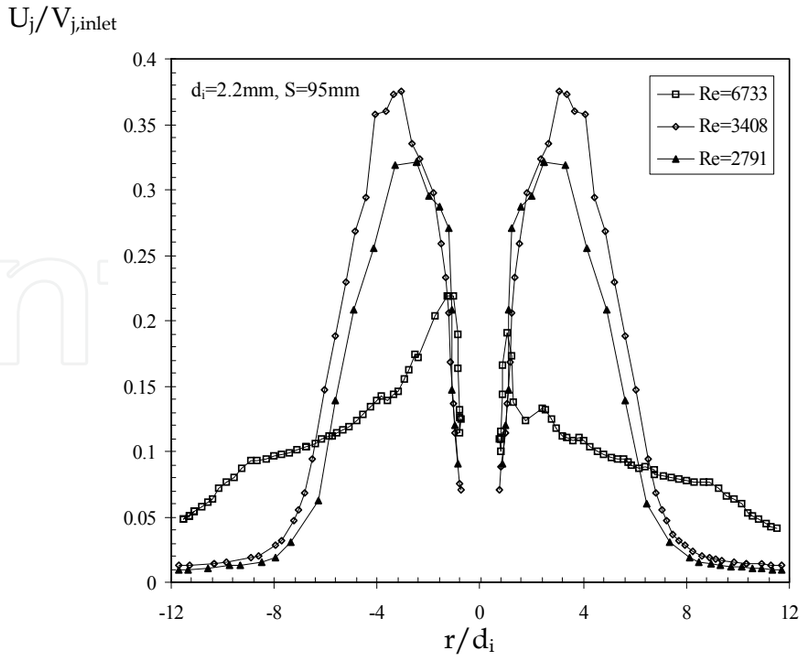

Fig. 7. Local evolution of the dimensionless radial velocity.

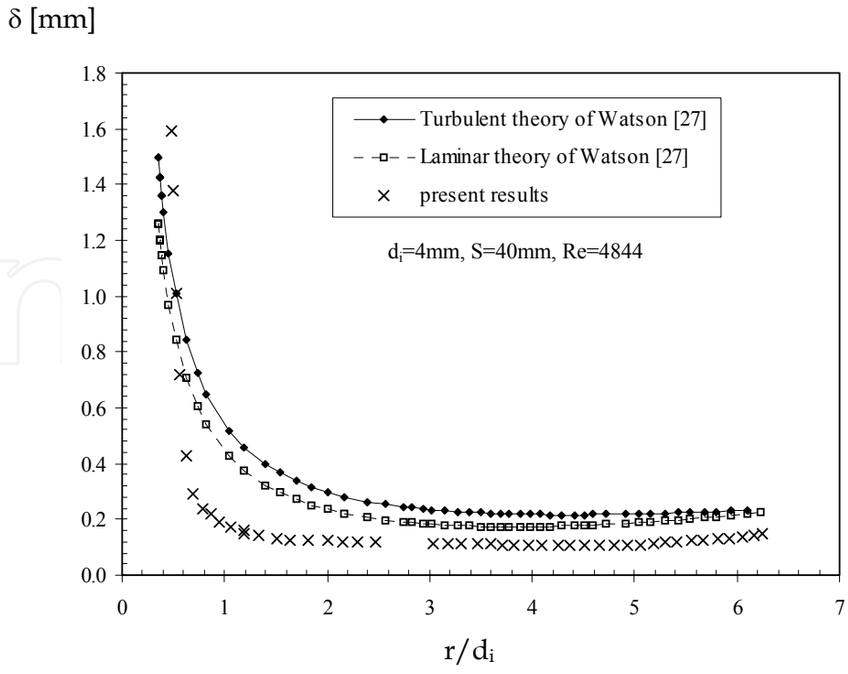

(a)

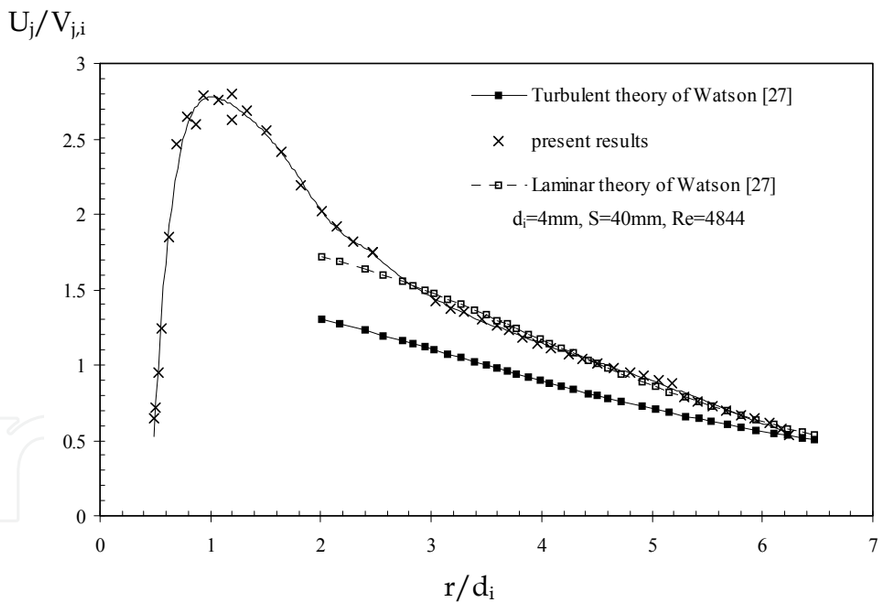

(b)

Fig. 8. Comparison of the experimental results with Watson's theory: (a) liquid layer depth (b) dimensionless radial mean velocity.

For the same radial position, Figure 7 shows effect of the hydraulic jump on the flow velocity. It shows that in the zone of the hydraulic jump, radial velocity is the lowest and approximately uniform for Re=3408 and Re=2791. For all data, the maximum dimensionless velocity is obtained for radius ranging from 2 to 4 times nozzle diameter. In the previous

work, Stevens and Webb (1989) found this maximum at r/d_i of 2.5 for the horizontal impinging jet on the vertical surface. Figure 7 also indicates that in the parallel flow, radial velocity is not uniform and it is lower than inlet jet velocity at the nozzle exit. The present results contradicts the assumption of some authors (Liu et al. 1989, Liu et al. 1991) assuming that the flow is fully developed before the hydraulic jump, and the free surface velocity is equal to the exit average jet velocity.

Experimental results are compared with the laminar and the turbulent theories predictions defined by Watson (1964) in figures 8a and b. It shows that laminar theory provides the best agreement with experimental data but sub-estimates the liquid layer depth. However, the turbulent theory underestimates liquid velocity along the radial direction and sub-estimates the liquid layer depth.

For all experiences showed in this section, it can be seen that when a circular liquid free jet strikes a flat plate, it spreads radially in very thin film along the heated surface, and the hydraulic jump that is associated with a Rayleigh-Taylor instability, can be appeared. Three distinct regions are identified and flow velocity is varied along the jet. Therefore, local distribution of heat flux and heat transfer coefficient is variable following the liquid layer depth and flow velocity.

There has been little information available in the published literature on local heat transfer for cooling using evaporation of impinging free liquid jet. The reason is that the liquid film spreads radially on the heated surface in very thin film, and determination of local heat flux on the wetted surface requires measurement of the temperature profiles along the axial and radial directions without perturbing the flow. Therefore, inverse heat conduction problem (IHCP) has been solved in order to determine locally distribution of thermal boundary conditions at the wetted surface using only temperatures measured inside the wall.

3. Determination of the thermal boundary conditions

In the previous work (Chen et al., 2001, Martin & Dulkravich, 1998, Louahlia-Gualous et al., 2003, Louahlia & El Omari, 2006), IHCP is used to estimate the thermal boundary conditions in various applications of science and engineering when direct measurements are difficult. IHCP could determine the precise results with numerical computations and simple instrumentation inside the wall.

In this study, experiments were investigates using a disk heated at its lower surface. The disk is 50 mm in diameter and 8 mm thick (Figure 9). It is thermally insulated with Teflon on all faces except the cooling face in order to prevent the heat loss. Liquid jet impactes perpendicularly in the center of the heat exchange surface (top surface of the disk). Temperatures inside the experimental disk are measured using 7 Chromel-Alumel thermocouples of 200 μm diameter (uncertainty of ±0.2°C). As shown in Figure 9, thermocouples are placed at 0.6 mm below the wetted surface at radial intervals of 3.5 mm.

The experimental disk is heated continually and the wall temperatures are monitored. When thermal steady state is reached, the heat exchange surface is quickly cooled with the liquid jet. Time-dependent local wall temperatures are recorded, until the experimental disk reaches a new steady state. The local surface temperature and heat flux are determined by solving IHCP using these measurements.

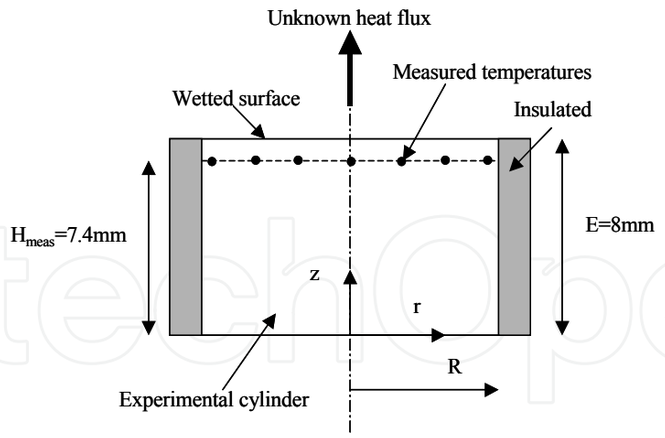

Fig. 9. Physical model.

Physical model of a unsteady heat conduction process is given by the following system of equations:

$$\frac{\rho C_p}{\lambda}\frac{\partial T(r,z,t)}{\partial t}=\frac{\partial^2 T(r,z,t)}{\partial r^2}+\frac{1}{r}\frac{\partial T(r,z,t)}{\partial r}+\frac{\partial^2 T(r,z,t)}{\partial z^2}, \tag{4}$$

where $0<r<R$, $0<z<E$

$$\frac{\partial T}{\partial r}(0,z,t)=0\text{, where } 0<t\le t_f,\ 0\le z\le E \tag{5}$$

$$\frac{\partial T}{\partial r}(R,z,t)=0\text{, where } 0<t\le t_f,\ 0\le z\le E \tag{6}$$

$$T(r,z,0)=T_0\text{, where : } 0\le r\le R,\ 0\le z\le E \tag{7}$$

$$\lambda\frac{\partial T}{\partial z}(r,E,t)=Q_w(r,E,t)\text{, where : } 0<t\le t_f,\ 0\le r\le R \tag{8}$$

$$T(r,0,t)=f(r,t)\text{, where : } 0<t\le t_f,\ 0\le r\le R \tag{9}$$

Distribution of local heat flux $Q_w(r,E,t)$ at the heat exchange surface (z=E) is unknown. It is estimated by solving the IHCP using temperatures $T_{meas}(r_n,z_n,t)$ measured at nodes (r_n, z_n) inside the disk (Figure 9). Solution of the inverse problem is based on the minimization of the residual functional defined as:

$$J(C(T),\lambda(T))=\sum_{n=1}^{N}\int_{t_0}^{t_f}\left[T(X_n,t;C(T),\lambda(T))-f_n(t)\right]^2 dt\rightarrow\min \tag{10}$$

where $T(r_n,z_n;Q_w)$ are temperatures at the sensor locations computed from the direct problem (4-9). Minimization is carried out by using conjugate gradient algorithm (Alifanov

et al., 1995). Heat flux $Q_w(r,E,t)$ is approximated in the form of a cubic B-spline and the IHCP is reduced to the estimation of a vector of B-Spline parameters. Conjugate gradient procedure is iterative. For each iteration, successive improvements of desired parameters are built. Descent parameter is computed using a linear approximation as follows:

$$\gamma^{it} = -\frac{\int_0^{t_f}\sum_{n=1}^{N_{meas}}\left[T^{it}(r_n,z_n,t;Q_w)-T_{meas}(r_n,z_n,t)\right]\theta^{it}(r_n,z_n,t;\delta Q_w)\,dt}{\int_0^{t_f}\sum_{n=1}^{N_{meas}}\theta^{it}(r_n,z_n,t;\delta Q_w)^2 dt} \tag{11}$$

Variation of temperature at the sensor locations $\theta^{it}(r_n,z_n,t;\delta Q_w)$ resulting from the variation of heat flux $\delta Q_w(r,E,t)$ is determined by solving variational problem. Variation of functional $J(Q_w)$ resulting from temperature variation is given by:

$$\delta J(Q_w,\delta Q_w) = \sum_{n=1}^{N_{meas}}\int_{t_0}^{t_f}\left[T(r_n,z_n,t,q_w)-T_{meas}(r_n,z_n,t)\right]\theta(r_n,z_n,t)dt \tag{12}$$

where $\theta^{it}(r_n,z_n,t;\delta Q_w)$ is determined at the sensor locations (r_n,z_n) by solving variational problem that defined by the following equations:

$$\frac{\rho C_p}{\lambda}\frac{\partial\theta(r,z,t)}{\partial t} = \frac{\partial^2\theta(r,z,t)}{\partial r^2}+\frac{1}{r}\frac{\partial\theta(r,z,t)}{\partial r}+\frac{\partial^2\theta(r,z,t)}{\partial z^2} \tag{13}$$

where $0\le r\le R$, $0\le z\le E$, $0<t\le t_f$

$$\frac{\partial\theta}{\partial r}(0,z,t)=0 \text{ , where } 0<t\le t_f,\ 0\le z\le E \tag{14}$$

$$\frac{\partial\theta}{\partial r}(R,z,t)=0 \text{ , where } 0<t\le t_f,\ 0\le z\le E \tag{15}$$

$$\theta(r,z,0)=0 \text{ , where : } 0\le r\le R,\ 0\le z\le E \tag{16}$$

$$\lambda\frac{\partial\theta}{\partial z}(r,E,t)=0 \text{ , where : } 0<t\le t_f,\ 0\le r\le R \tag{17}$$

$$\theta(r,0,t)=0 \text{ , where : } 0<t\le t_f,\ 0\le r\le R \tag{18}$$

3.1 Lagrangian functional and adjoint problem

Using Lagrange multiplier method, Lagrangian functional is defined as:

$$J(C(T),\lambda(T)) = \sum_{n=1}^{N}\int_{t_0}^{t_f}\left[T(X_n,t;C(T),\lambda(T))-f_n(t)\right]^2 dt \to \min$$

$$+\int_0^{t_f}\int_0^{R}\psi(r,z,t)\left[\frac{\lambda}{r}\frac{\partial}{\partial r}\left(r\frac{\partial T}{\partial r}\right)+\lambda\frac{\partial^2 T}{\partial z^2}-\rho C_p\frac{\partial T}{\partial t}\right]dr\,dz\,dt$$

$$+\int_0^{t_f}\int_0^{R}\xi(r,t)\left[T(r,0,t)-f(r,t)\right]dr\,dt+\int_0^{t_f}\int_0^{E}\omega(z,t)\,\lambda\frac{\partial T}{\partial\phi}(R,z,t)\,dz\,dt$$

$$+\int_0^{t_f}\int_0^{R}\gamma(r,t)\left[\lambda\frac{\partial T}{\partial z}(r,E,t)+Q_w(r,E,t)\right]dr\,dt+\int_0^{t_f}\int_0^{E}\mu(z,t)\left[\lambda\frac{\partial T}{\partial r}(0,z,t)\right]dz\,dt$$

$$+\int_0^{R}\int_0^{E}\eta(r,z)\left[T(r,z,0)-T_0\right]dr\,dz \tag{19}$$

Let $\psi(r,z,t)$, $\xi(r,t)$, $\omega(z,t)$, $\mu(z,t)$, $\eta(r,z)$ and $\gamma(r,t)$ be the Lagrange multipliers. The necessary condition of the optimization problem is obtained from the following equation:

$$\delta L(Q_w,\delta Q_w)=0 \tag{20}$$

where $\delta L(Q_w,\delta Q_w)$ is the variation of Lagrangian functional. Equation (19) requires that all coefficients of the temperature variation $\theta(r,z,t)$ be equal to 0. To satisfy this condition the necessary conditions of optimization are defined in the form of adjoint problem.

$$-\frac{\rho C_p}{\lambda}\frac{\partial\psi(r,z,t)}{\partial t}=\frac{\partial^2\psi}{\partial r^2}-\frac{1}{r}\frac{\partial\psi}{\partial r}+\frac{1}{r^2}\psi+\frac{\partial^2\psi}{\partial z^2}+S(r,z,t) \tag{21}$$

where: $S(r,z,t)=-\sum_{n=1}^{N_{meas}}\left\{\delta(r,r_n;z,z_n)\times\left[T(r_n,z_n,t;Q_w)-T_{meas}(r_n,z_n,t)\right]\right\}$,

$$0\le r\le R,\ 0\le z\le E,\ 0<t\le t_f$$

$$\frac{\partial\psi}{\partial r}(0,z,t)=\frac{\psi}{r}(0,z,t),\ \text{where}\ 0<t\le t_f,\ 0\le z\le E \tag{22}$$

$$\frac{\partial\psi}{\partial r}(R,z,t)=\frac{\psi}{r}(R,z,t),\ \text{where}\ 0<t\le t_f,\ 0\le z\le E \tag{23}$$

$$\psi(r,z,t_f)=0,\ \text{where}:\ 0\le r\le R,\ 0\le z\le E \tag{24}$$

$$\lambda\frac{\partial\psi}{\partial z}(r,E,t)=0,\ \text{where}:\ 0<t\le t_f,\ 0\le r\le R \tag{25}$$

$$\psi(r,0,t)=0,\ \text{where}:\ 0<t\le t_f,\ 0\le r\le R \tag{26}$$

where $\psi(r,z,t)$ is the Lagrange multiplier,

$$J(C(T),\lambda(T)) = \sum_{n=1}^{N} \int_{t_0}^{t_f} \left[T(X_n,t;C(T),\lambda(T)) - f_n(t)\right]^2 dt \rightarrow \min$$

is the Dirac Function, $S(r,z,t)$ is the deviation between temperature measurements and computed temperatures. $S(r,z,t)$ is equal to 0 everywhere in the physical domain except at sensor locations (r_n,z_n).

The Dirac function is defined by

$$J(C(T),\lambda(T)) = \sum_{n=1}^{N} \int_{t_0}^{t_f} \left[T(X_n,t;C(T),\lambda(T)) - f_n(t)\right]^2 dt \rightarrow \min \quad (27)$$

where $\delta(0)=1$, $\delta(r)=0$ for $r \neq 0$ and $\delta(z)=0$ for $z \neq 0$

If the direct problem and the adjoint problem are verified, variation of the Lagrangian functional becomes:

$$\delta \mathbf{L}(Q_w,\delta Q_w) = -\int_0^{t_f} \int_0^{R} \psi(r,E,t)\, \delta Q_w(r,E,t)\, dr\, dt \quad (28)$$

Vector gradient can be verified by the following equation:

$$J'_{Q_w}(r,E,t) \quad = -\psi(r,E,t) \quad (29)$$

3.2 Gradient vector computation

Variation of functional $J(Q_w)$ can be approximated in the form:

$$\delta J(Q_w,\delta Q_w) = -\int_0^{t_f} \int_0^{E} \int_0^{R} \left[\frac{\rho C_p}{\lambda} \frac{\partial \psi(r,z,t)}{\partial t} + \frac{\partial^2 \psi}{\partial r^2} - \frac{1}{r}\frac{\partial \psi}{\partial r} + \frac{1}{r^2}\psi + \frac{\partial^2 \psi}{\partial z^2} \right] \theta(r,z,t)\, dr\, dz\, dt \quad (30)$$

Integration by parts gives, the variation of functional becomes using Eqs (21-26):

$$\delta J(Q_w,\delta Q_w) = \int_0^{t_f} \int_0^{R_2} \left[-\lambda \frac{\partial \psi}{\partial z}\theta(r,t) + \lambda \psi(r,t) \frac{\partial \theta(r,t)}{\partial z} \right] dr dt \quad (31)$$

Substituting Eqs. (25) and (17) into Eq. (31), $\delta J(q_w,\delta q_w)$ becomes:

$$\delta \mathbf{J}(Q_w,\delta Q_w) = -\int_0^{t_f} \int_0^{R} \psi(r,E,t)\, \delta Q_w(r,E,t)\, dr\, dt$$

$$= \delta \mathbf{L}(Q_w,\delta Q_w) \quad (32)$$

Variation of functional is defined as:

$$\delta J(Q_w, \delta Q_w) = \int_0^{t_f} \int_0^{R_2} J'_{Q_w}(r, E, t)\, \delta Q_w(r, E, t)\, dr\, dt \tag{33}$$

Equations (32) and (33) imply that:

$$J'_{Q_w}(r, E, t) = -\psi(r, E, t) \tag{34}$$

Vector gradient can verified the following equation:

$$J'_{Q_w}(r, E, t) = -\psi(r, E, t) \tag{35}$$

3.3 Algorithm

The following iterative procedure is adopted to solve the inverse heat conduction problem:

i. solution of the direct problem,
ii. calculation of the residual functional,
iii. solution of the adjoint problem,
iv. calculation of the components of the functional gradient,
v. calculation of the parameter in descent direction,
vi. calculation of the component of descent direction,
vii. solution of the variational problem to determine the descent parameter,
viii. the new value of the heat flux density is corrected.

If the convergence criteria is not satisfied the iterative procedure is repeated until the functional is minimized. The minimal value of the functional depends on the temperature measurement errors.

The direct problem, adjoint problem, and variational problem are solved using the control volume method (Patankar, 1980) and the implicit fractional-step time scheme proposed by (Brian, 1961).

3.4 Regularization

The inverse problem is ill-posed and numerical solution depends on the fluctuation occurring in the measurements. The iterations are stopped at the optimal value of the residual functional which satisfies the criteria:

$$J(Q_w) = \frac{1}{2} \int_0^{t_f} \sum_{n=1}^{N_{meas}} \sigma^2(r_n, z_n, t)\, dt \tag{36}$$

Here, $\sigma^2(r_n, z_n, t)$ is the standard deviation of measurement errors for the temperatures measured at locations (r_n, z_n).

4. Inverse estimation of the boundary conditions

4.1 Numerical verification of the solution procedure

The numerical procedure is verified by using a known heat flux varying with time and the radius of the disk. Heat flux is imposed at the top surface of the disk (z = E) as shown in Figure 10 by the continuous curve. The bottom surface (z=0) is assumed to be at the constant

temperature of T(r,0,t)= 40°C. For each numerical application, time step size is chosen with respect to delta Fourier number condition defined by the following equation:

$$\Delta Fo = \frac{\lambda}{\rho C_p} \frac{\Delta t}{\left(E - H_{meas}\right)^2} \geq 0.001 \tag{37}$$

The delta Fourier number is based on the sensor depth, thermal characteristics of the solid, and time step (Williams & Beck, 1995, Beck & Brown, 1996).

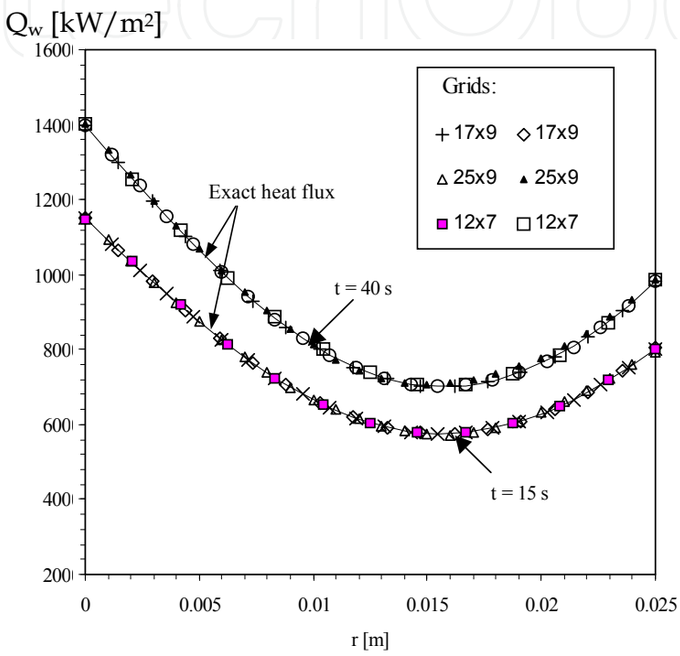

Fig. 10. Heat flux variation with radius on the top surface. Verification of the IHCP: solid line ("measurements"), symbols ("estimations using inverse method").

In order to validate inverse estimation procedure, it is assumed that temperatures calculated from the direct problem at the measurement points are used as the measured temperatures ($T_{meas}(r_n, z_n, t) = f_n(r_n, z_n, t)$) for solving ICHP. Figure 10 shows that the estimated heat flux is closed with the exact heat flux for different times. This validation is carried out for the number of approximation parameters equal to 9x9. The maximum deviation between the computed temperatures and the simulated measured temperatures is of ±0.03°C. The evolution of the residual functional $J(Q_w)$ is a function of the number of iterations that are continued till the convergence criteria is satisfied.

4.2 Inverse estimation of evaporation local heat transfer for jet impingement

4.2.1 Evaporation local heat transfer for unsteady state

For inlet Reynolds number of 7600, Figure 11 shows an example of temporal temperatures measured for different radial locations at 0.6 mm below the heat exchange surface. During experiments, heat flux imposed inside the experimental disk is 45 W, the nozzle-heat exchange surface spacing is 30 mm, and the liquid inlet temperature is 42°C. At the steady

state, wall temperatures are 78°C. When the heat exchange surface is wetted, the wall temperatures decrease continually and reach a stable value during a short period. Temperature at the stagnation zone is lower than the temperature measured far from the impingement zone. IHCP is solved using temperatures measured at H_{meas} = 7.4mm (Figure 11) in order to estimate the local surface temperature and heat flux. These local thermal characteristics are estimated using the temperatures measured at the bottom surface (z=0) as the boundary condition to solve the direct problem.

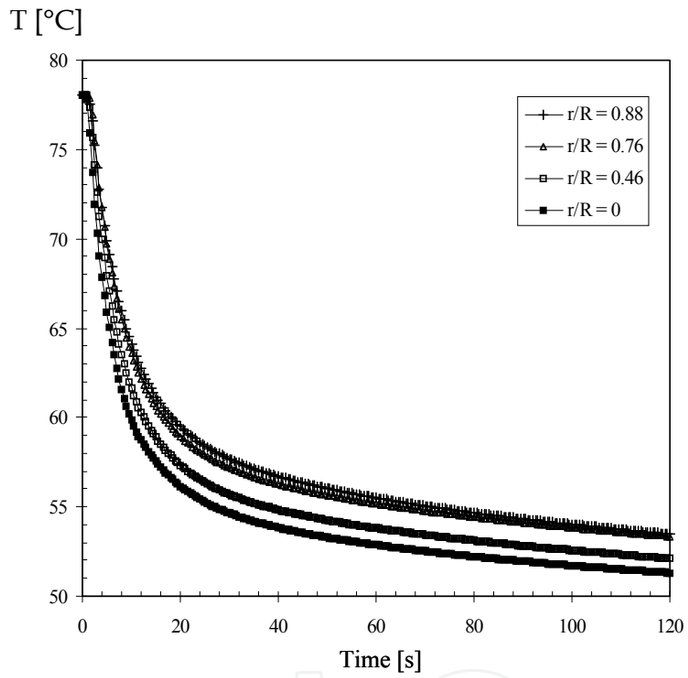

Fig. 11. Temperatures measured inside the solid at z = H_{meas}.

Figures 12 and 13 show, respectively, the unsteady evolution of the predicted surface heat flux and temperature at different radial locations on the cooling surface (z = E =8 mm). Surface temperature is low in the stagnation and in impingement zone where heat flux is high. The difference between the wall and liquid temperatures is high at the moment when the liquid jet impinges the heat exchange surface. After this, heat flux decreases with time and follows the same trend for each radial location. Heat flux decreases after the impingement zone because liquid spreads along the radial direction as a very thin film. The experimental data for each radial location and inlet Reynolds number, follows the same trend. For brevity, theses curves are not shown in this figure.

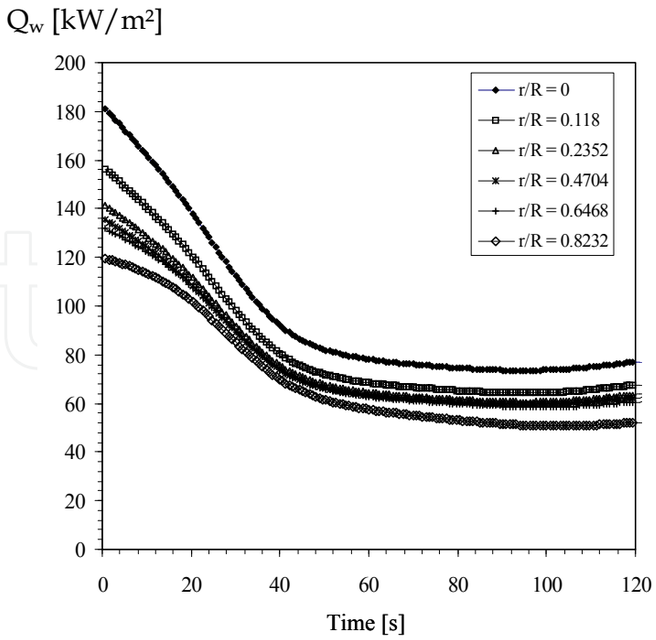

Fig. 12. Heat flux inversely predicted at the top surface.

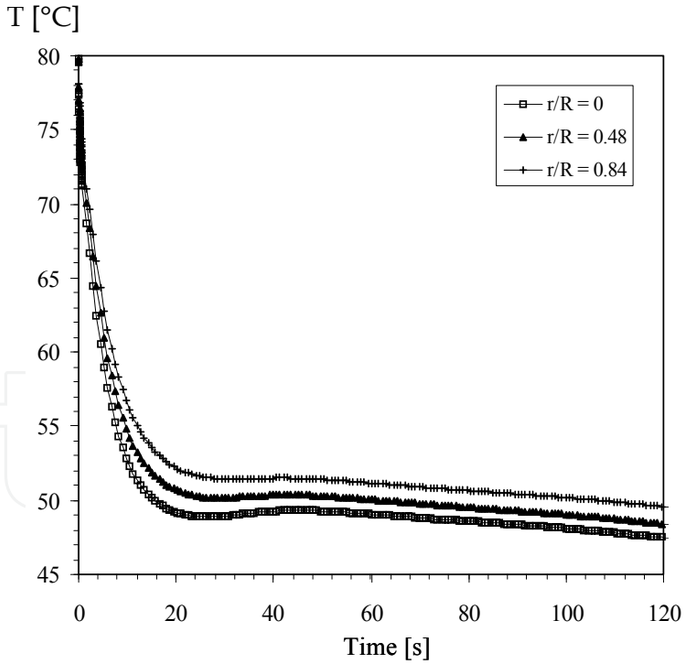

Fig. 13. Temperatures inversely predicted at the top surface.

For both sides of the disk, radial distributions of the surface heat flux and heat transfer coefficients are presented in Figures 14a and 14b for different times. Local heat flux and heat transfer coefficients are not uniform along the radial direction, and they are high in the impingement zone.

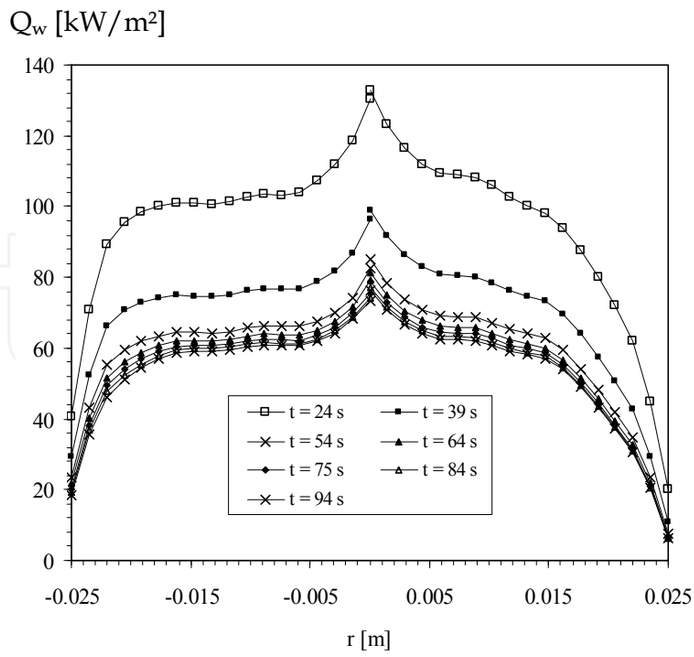

(a)

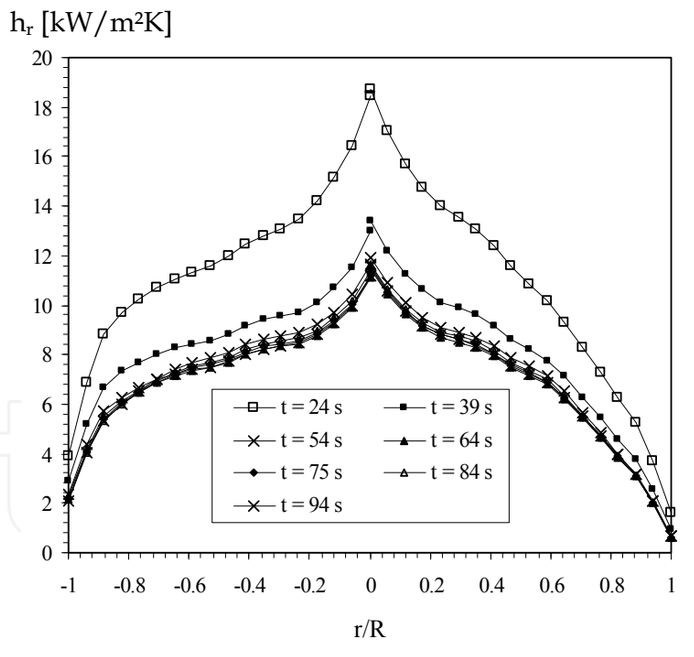

(b)

Fig. 14. Radial distribution inversely predicted at the top surface (z = E) : (a) heat flux and (b) heat transfer coefficient.

After the impingement zone, heat transfer decreases because the liquid jet covers the entire heat exchange surface. Therefore, local liquid flow rate decreases in spite of the decrease of the film thickness. When the radius r becomes higher than approximately 0.018 mm, heat

transfer is reduced because of the hydraulic jump formation where the velocity of the flow becomes relatively negligible. At each time, the local heat flux and heat transfer coefficient follow the same trend. Beyond 64s, the curves of the heat flux and those of the heat transfer coefficient are independent on the time because of the steady state.

4.2.2 Evaporation local heat transfer for steady state

For steady state, Figure 15 shows the local distributions of the surface temperature and heat transfer coefficient. For each radial location, the local heat transfer coefficient is determined from the surface heat flux and temperature as follows:

$$h_r = \frac{Q_{w,r}}{T_{s,r} - T_e} \tag{38}$$

where h_r is the local heat transfer coefficient, $Q_{w,r}$ is the local heat flux, $T_{s,r}$ is the local surface temperature, and T_e is the liquid temperature at the nozzle exit.

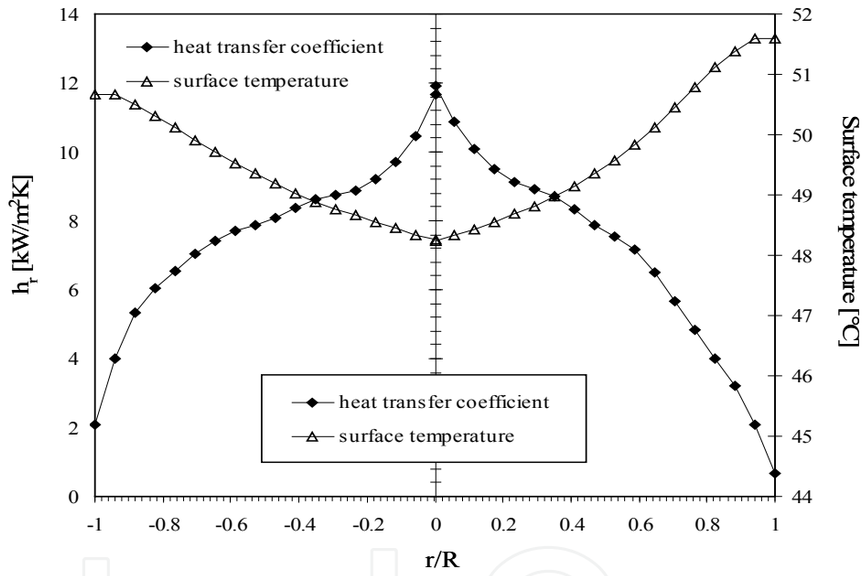

Fig. 15. Local thermal characteristics for steady state.

The surface temperature is low in the stagnation zone compared to all the zones of the heat exchange surface. The maximum heat transfer coefficient is occurred in the stagnation point. For different flow rates, Figure 16 illustrates the unsteady evolution of the surface temperatures for two radial locations. The first one is at the stagnation point where the surface temperature is low. The second is far from the impingement zone (at r=0.82R), where the heat transfer coefficient is deteriorated because of the hydraulic jump. The surface temperature in this zone is higher than in the stagnation point. It is shown that the surface temperature is less influenced by the flow rate at the stagnation zone than for r=0.82R where the film thickness is small. The normalized heat transfer coefficient is determined as the fraction of the local heat transfer coefficient and h_0 that is defined at the stagnation zone (Figure 17). For each tested flow rate, the heat transfer coefficient decreases from h_0 to 50% of h_0 at radial location approximately equal to 0.6R.

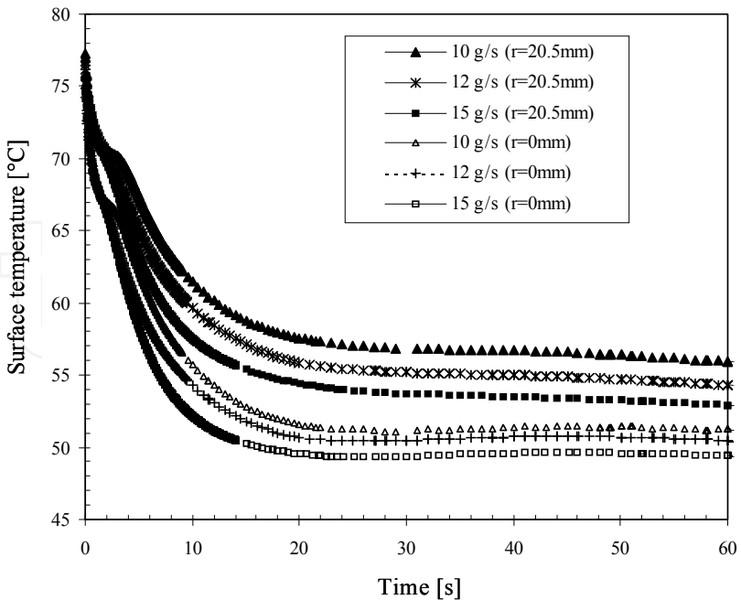

Fig. 16. Local surface temperatures inversely predicted at the top surface.

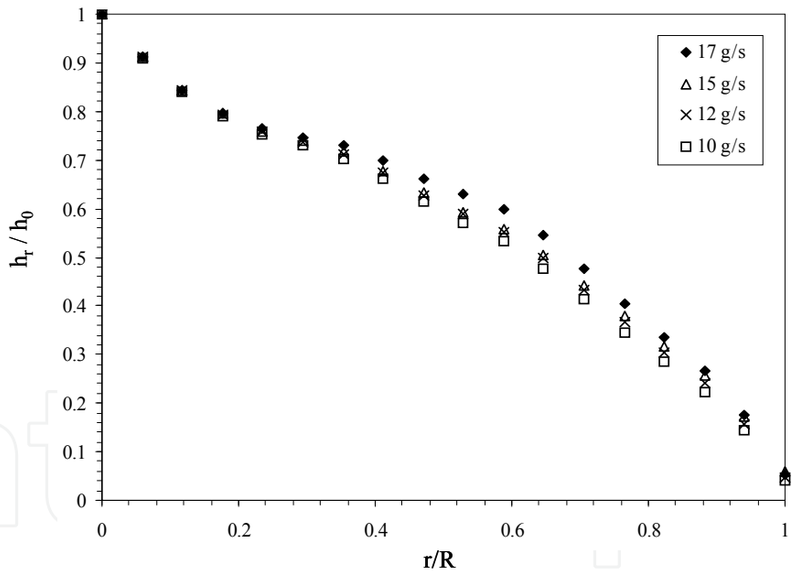

Fig. 17. The normalized heat transfer coefficient distribution as a function of water jet flow rate.

5. Conclusion

Various theoretical and experimental investigations on convective local heat transfer have been published in the literature where local heat transfer coefficient is determined from total heat flux or using direct estimation (Fourier's law). In this case, heat flux is assumed to be dissipated only in the axial direction and constant along the heat exchange surface.

In this work, local heat transfer is analyzed by solving inverse heat conduction problem and using only sensors responses placed inside the experimental disk. Iterative regularization method is used to solve the inverse problem under analysis. Solution procedure is based on the conjugate gradient method used to minimize the residual functional and the residual discrepancy principal as the regularizing stopping criterion.
For each radial location, local heat transfer coefficient is determined using local heat flux and surface temperature. The heat flux and heat transfer coefficient are high in the impingement zone and decrease after this zone because liquid flow spreads along the radial direction as a very thin film. At each time, surface temperature is low in the stagnation zone and the highest heat transfer coefficient occurs in the stagnation zone and falls off with the radial location because local flow rate decreases. For different tested flow rates, the heat transfer coefficient decreases from h_0 to 50% of h_0 at the radial location approximately equal to 0.6R.

6. References

Alifanov, O.M., Artyukhin, E.A. and Rumyantsev, S.V., (1995). Extreme Methods for Solving Ill-Posed Problems with Applications to Inverse Heat Transfer Problems, Begell House, New York.

Baonga, J.B., Louahlia-Gualous, H. & Imbert, M. (2006). Experimental study of the hydrodynamic and heat transfer of free liquid jet impinging a flat circular heated disk, *Applied Thermal Engineering*, Vol. 26, pp. 1125-1138.

Brian, P.L.T., (1961). A finite-difference method of higher order accuracy for solution of three dimensional transient heat conduction, *A.I.Ch.E. Journal*, vol. 7, pp. 367-370.

Chen, R.H., Chow, L.C. & Navedo, J.E. (2002). Effects of spray characteristics on critical heat flux in subcooled water spray cooling, *Int. J. Heat and Mass Transfer*, Vol. 45, pp. 4033-4043.

Chen, H.T., Lin, S.Y. and Fang, L.Ch., (2001). Estimation of surface temperature in two dimensional inverse heat conduction problems, *Int. J. of Heat and Mass Transfer,* vol. 44, pp. 1455-1463.

Elison, B. & Webb, B.W. (2003). Local heat transfer to impinging liquid jets in the initially laminar, transitional, and turbulent regimes, *Int. J. Heat Mass Transfer,* Vol. 37, pp. 1207-1217.

Fabbri, M., Jiang, Sh. & Dhir, V.K. (2003). Experimental investigation of single-phase micro jets impingement cooling for electronic applications, *Proc. Of Heat Transfer Conference ASME*, pp. 1-10.

Liu, X., Lienhard J.H. & Lombara, J.S. (1991). Convective heat transfer by impingement of circular liquid jets, *J. of Heat Transfer, Transaction of the ASME*, Vol. 113, pp. 571-582.

Liu, X. & Lienhard J.H. (1989). Liquid jet impingement heat transfer on a uniform flux surface, *National Heat Transfer Conference*, Vol. 106, pp. 523-530.

Lin, L. & Ponnappan, R. (2004). Critical heat flux of Multi-nozzle spray cooling, *J. of Heat Transfer, Transaction of the ASME*, Vol. 126, pp. 482-485.

Liu, Z.H. & Zhu, Q.Z. (2004). Prediction of critical heat flux for convective boiling of saturated water jet impinging on the stagnation zone, *J. of Heat Transfer, Transaction of the ASME*, Vol. 124, pp. 1125-1130

Louahlia-Gualous, H., Panday, P.K. and Artioukhine, E., (2003). Inverse determination of the local heat transfer coefficients of nucleate boiling on a horizontal cylinder, *Trans. ASME, J. Heat Transfer*, vol. 125, pp. 1087-1095.

Louahlia-Gualous, H. & Baonga, J.B. (2008). Experimental study of unsteady local heat transfer for impinging miniature jet, *Heat Transfer Engineering*, Vol. 29, N°. 2, pp.782-792.

Louahlia-Gualous H. & El Omari, L. (2006). Local heat transfer for the evaporation of a laminar falling liquid film on a cylinder - Experimental, numerical and inverse heat conduction analysis, *Numerical Heat Transfer, Part A: Applications*, Vol. 50 N° 7, p. 667-688.

MA, C.F., Zheng, Q., Lee, S.C. & Gomi, T. (1997). Impingement heat transfer and recovery effect with submerged jets of large Prandtl number liquid-I. Unconfined circular jets, *Int. J. Heat Mass Transfer*, Vol. 40, No. 6 pp. 1481-1490.

MA, C.F., Zheng, Q., Sun, H., Wu, K., Gomi, T. & Webb, B.W. (1997). Local characteristics of impingement heat transfer with oblique round free-surface jets of large Prandtl number liquid, *Int. J. Heat Mass Transfer*, Vol. 40, No. 10, pp. 2249-2259

Martin, T.J. & Dulkravich, G.S., (1998) Inverse determination of steady heat convection coefficient distributions, *J. of Heat Transfer, Transaction of the ASME*, Vol. 120, pp. 328-334.

Oliphant, K., Webb, B.W., McQuay, M.Q., (1998). An experimental comparison of liquid jet array and spray impingement cooling in the non-boiling regime, *Exp. Thermal and Fluid Science,* Vol. 18, pp. 1-10.

Pan, Y. & Webb, B.W., (1995). Heat transfer characteristics of array of free-surface liquid jets, *Transaction of the ASME,* Vol. 177, pp. 878-884

Patankar, S.V., (1980). Numerical Heat Transfer and Fluid Flow, Mc Graw Hill, New York.

Siba, E.A., Ganesa-Pillai, M., Harris, K.T. & Haji-Sheikh, A. (2003) Heat transfer in a high turbulence air jet impinging over a flat circular disk, *J. of Heat Transfer, Transaction of the ASME*, Vol. 125, pp. 257-265.

Stevens, J. & Webb, B.W. (1989). Local heat transfer coefficients under an axisymmetric, single-phase liquid jet, *National Heat Transfer Conference*, Vol. 11, pp. 113-119.

Stevens, J., & Webb, B.W. (1993). Measurements of flow structure in the radial layer of impinging free surface liquid jets, *Int. J. Heat Mass Transfer*, Vol. 36, N°.15, pp. 3751-3758.

Stevens, J., & Webb, B.W. (1992). Measurements of the free surface flow structure under an impinging, free liquid jet, *Journal of Heat Transfer, Transaction of ASME*, Vol. 114, pp. 79-84.

Stevens,J. & Webb, B.W. (1989). Local heat transfer coefficients under an axisymmetric, single-phase liquid jet, *American society Mechanical Engineers. Heat Transfer Division*, Vol. 111 pp. 113-119.

Stevens, J. & Webb, B.W., (1991). Local heat transfer coefficients under an axisymmetric, single-phase liquid jet, *Journal of Heat Transfer*, Vol. 113, pp. 71-78.

Watson, E.J. (1964). The radial spread of a liquid over horizontal plane, *J. Fluid Mech*. Vol. 20, pp. 481-500.

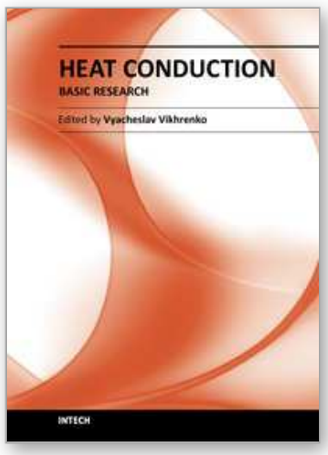

Heat Conduction - Basic Research

Edited by Prof. Vyacheslav Vikhrenko

ISBN 978-953-307-404-7
Hard cover, 350 pages
Publisher InTech
Published online 30, November, 2011
Published in print edition November, 2011

The content of this book covers several up-to-date approaches in the heat conduction theory such as inverse heat conduction problems, non-linear and non-classic heat conduction equations, coupled thermal and electromagnetic or mechanical effects and numerical methods for solving heat conduction equations as well. The book is comprised of 14 chapters divided into four sections. In the first section inverse heat conduction problems are discuss. The first two chapters of the second section are devoted to construction of analytical solutions of nonlinear heat conduction problems. In the last two chapters of this section wavelike solutions are attained.The third section is devoted to combined effects of heat conduction and electromagnetic interactions in plasmas or in pyroelectric material elastic deformations and hydrodynamics. Two chapters in the last section are dedicated to numerical methods for solving heat conduction problems.

InTech Europe
University Campus STeP Ri
Slavka Krautzeka 83/A
51000 Rijeka, Croatia
Phone: +385 (51) 770 447
Fax: +385 (51) 686 166
www.intechopen.com

InTech China
Unit 405, Office Block, Hotel Equatorial Shanghai
No.65, Yan An Road (West), Shanghai, 200040, China
中国上海市延安西路65号上海国际贵都大饭店办公楼405单元
Phone: +86-21-62489820
Fax: +86-21-62489821

IntechOpen